Safety, Reliability, Risk, Resilience and Sustainability of Structures and Infrastructure
12th Int. Conf. on Structural Safety and Reliability, Vienna, Austria, 6–10 August 2017
Christian Bucher, Bruce R. Ellingwood, Dan M. Frangopol (Editors)

Extraction of Building Damage due to 2016 Kumamoto Earthquake from PALSAR-2 Data

Fumio Yamazaki[a], Wen Liu[a] and Luis Moya[b]

[a] Department of Urban Environment Systems, Chiba University, Japan.
[b] International Research Institute of Disaster Science, Tohoku University, Japan.

Abstract: A series of earthquakes with Mw7.0 as the main-shock hit Kumamoto prefecture in Kyushu Island, Japan in April 2016. In this study, L-band Synthetic Aperture Radar (SAR) data acquired by PALSAR-2 sensor onboard ALOS-2 satellite were used to extract changes on the earth surface. Using a co-event PALSAR-2 pair dataset, the authors calculated the spatial coherence values of SAR backscattering echoes. By the obtained coherence image, extensive building damage areas were clearly highlighted. The extracted building damage distribution was compared with the result from airborne LiDAR data.

1 Introduction

Information gathering after a large-scale natural disaster is very important in emergency response and recovery activities. But the access to the affected areas is often hindered by the disruption of road networks and telecommunication systems. In this situation, remote sensing technologies have been employed to assess the extent and degree of various damages [1-3]. There are mainly two categories of remote sensing from the sensor type: passive (optical and thermal sensors) and active (mainly radar sensors). Optical satellite systems work in the daytime and cannot observe objects under cloud-cover conditions. However, a radar system as Synthetic Aperture Radar (SAR) overcomes this problem and can be used all day and under all weather conditions [4].

Various high-resolution optical and SAR satellites have been in operation in the last decade and they were employed to observe affected areas after major natural disasters, such as the 2011 Tohoku, Japan earthquake and tsunami [5-6], the 2011 central Thailand flood [7], the 2013 Haiyan, Philippines typhoon [8], and the 2015 Gorkha, Nepal earthquake [9]. The acquired satellite data provided the information on inaccessible affected areas.

Various aerial surveying technologies have also been developed in the last few decades, such as digital aerial cameras, LiDAR (Light Detection And Ranging), and more recently, unmanned aerial vehicles (UAVs, drones). The images acquired by digital aerial cameras have much higher radiometric resolution than those from analogue cameras, and thus they have been extensively used in recent natural disasters [10]. LiDAR is the most costly but the most accurate method to acquire digital surface models (DSMs), and hence it has been used to develop detailed digital elevation models (DEMs) and 3D configuration of buildings [11].

In this paper, SAR imagery data acquired before and after the 2016 Kumamoto, Japan earthquake are employed to extract building damage based on coherence values. Two temporal LiDAR digital surface models (DSMs) are also introduced as validation data.

2 The 2016 Kumamoto Earthquake Sequence

A Mw6.2 earthquake hit the Kumamoto prefecture in Kyushu Island, Japan on April 14, 2016 at 21:26 (JST). A considerable amount of structural damages and human casualties had been reported due to this event, including 9 deaths [12]. The epicenter was located in the Hinagu fault with a shallow depth.

On April 16, 2016 at 01:25 (JST), about 28 hours after the first event, another earthquake of Mw7.0 occurred in the Futagawa fault, closely located with the Hinagu fault. Thus, the first event was called as the "foreshock" and the second one as the "main-shock". The epicenters of the both events were located in Mashiki Town (about 33-thousand population), to the east of Kumamoto City (about 735-thousand population). The total number of aftershocks (larger than magnitude 3.5) reached 333 times as of December 6, 2016, eight months after the fore-shock. This number is the largest among recent inland (crustal) earthquakes in Japan [13].

Figure 1 shows the location of these causative faults and Japanese national GNSS Earth Observation Network System (GEONET) stations in the source area [14]. Note that the GEONET system has about 1,300 stations covering Japan's territory uniformly. The displacement of 75 cm to the east-northeast (ENE) was observed at the Kumamoto station while that of 97 cm to the southwest (SE) was recorded at the Choyo station during the main-shock. These observations validated the right-lateral strike-slip mechanism of the Futagawa fault.

The peak ground acceleration (PGA) and the peak ground velocity (PGV) recorded at the KiK-net Mashiki station (KMMH16) were 925 cm/s^2 and 92 cm/s in the foreshock while those were 1,313 cm/s^2 and 132 cm/s in the main-shock [15]. These values are quite large among recent earthquake records in Japan. Extensive impacts due to strong shaking and landslides were associated by the Kumamoto earthquake sequence, such as collapse of buildings and bridges, and suspension of road and railway networks [16]. A total of fifty (50) direct deaths were accounted by the earthquake sequence, mostly due to the collapse of wooden houses in Mashiki Town and landslides in Minami-Aso Village.

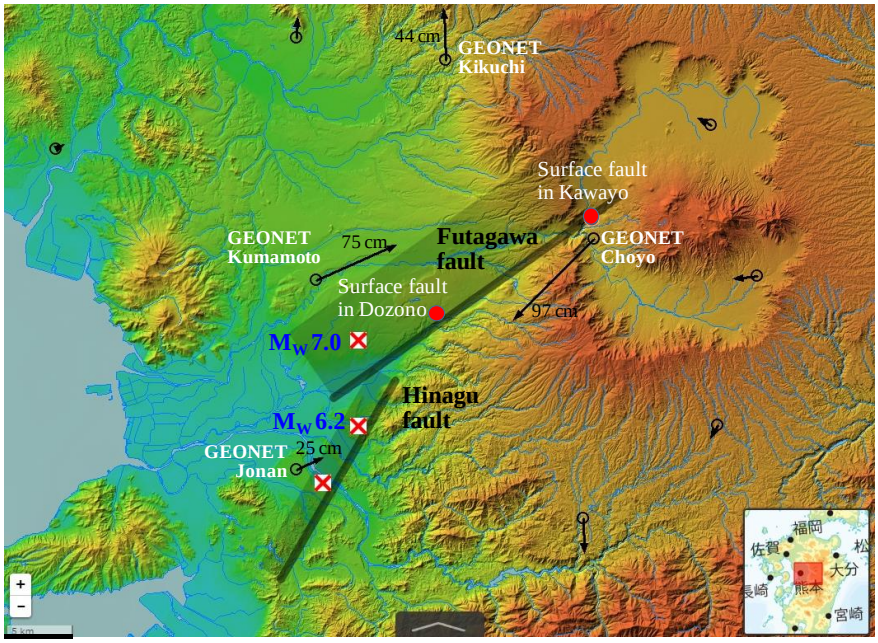

Figure 1: Location of causative faults and GNSS stations in the 2016 Kumamoto earthquake

3 Imagery and GIS Data Used

The study area focuses on the affected densely inhabited districts (DIDs) in Mashiki Town as shown in **Figure 2**. Soon after the occurrence of the April-14 earthquake, PALSAR-2 onboard ALOS-2 satellite carried out emergency observation. Two PALSAR-2 images, one just after the foreshock (April 15, 2016) and one after the main-shock (April 29, 2016), were used in this study to extract changes caused by the main-shock on April 16. These images were acquired in the StripMap mode by the HH polarization from a descending path with left-look. The incidence angle was almost the same for the two images, 32.4 degrees, and the resolution was 1.43 m to the range-direction and 1.74 m to the azimuth-direction. They were provided as the level 1.1 data in the slant range, which were represented by complex *I* and *Q* channels to preserve the amplitude and phase information.

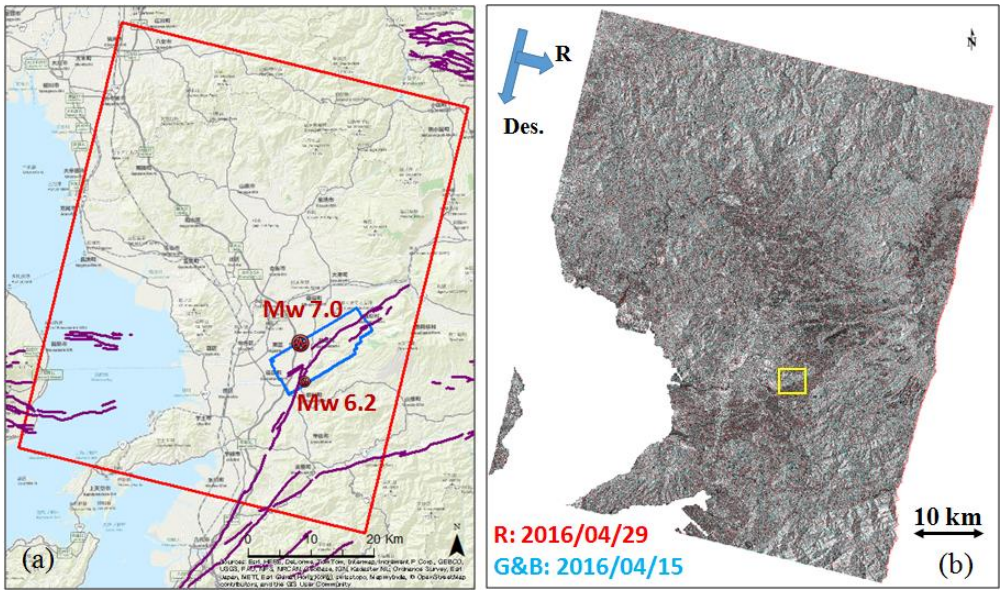

Figure 2: PALSAR-2 images used in this study. (a) Location of SAR images (red square) and LiDAR data (blue polygone). (b) Color composite of backscattering coefficients with the target area in Mashiki Town (yellow square).

Several pre-processing steps were applied before change detection. The pair data were registered in a sub-pixel level. A globally available digital elevation model (Shuttle Radar Topography Mission: STRM) was used to compensate the image distortion caused by the terrain heights. Then they were projected to a World Geodetic System (WGS) 84 reference ellipsoid with a re-sampled square pixel of 2.5 m. The amplitude information was converted to the backscattering coefficient (sigma naught, σ_0) in the dB unit, using the calibration factor [17]. The color composite of the backscattering coefficient of the two SAR images is shown in the figure.

Figure 3 shows an aerial photograph [14] taken at the noon time (12:21) of April 16, 2016 by the Geospatial Information Authority of Japan (GSI) for the central Mashiki Town and the land-cover map of the same area by JAXA [18], which was introduced to extract urban land-cover from the SAR images. About 45% of the target area was classified as "urban" where buildings exist. The target area for change detection was restricted to only this urban land-cover since the change in vegetation may become a cause of errors. In the close-up of the aerial photo, many blue plastic sheets covering the roofs of houses were seen, which represent the damage situation of them.

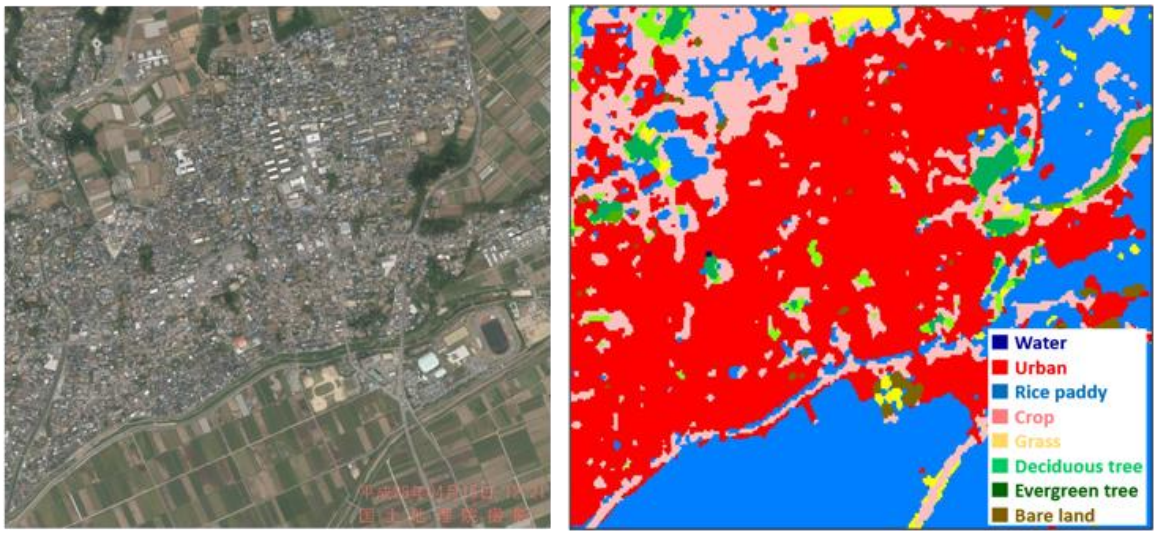

(a) (b)

Figure 3: Aerial photograph of the central Mashiki Town taken at 12:21 (local time) on April 16, 2016, soon after the main-shock, by the GSI (a); the land-use and land-cover map of the same area by JAXA (b).

4 Change Detection based on Coherence and its Validation

The objective of this study is to grasp the damage situation soon after the occurrence of a disaster. Thus, a simple extraction method using threshold values of the coherence function was adopted. The coherence (γ) is the interferometric correlation between two SAR complex data, which is calculated by the ratio between coherent and incoherent summations as Eq. (1).

$$\gamma = \frac{\sum C_1 C_2}{\sqrt{\sum |C_1|^2}\sqrt{\sum |C_1|^2}} \tag{1}$$

where C is a complex number with phase (ϕ) and magnitude (A) [19]. The estimated absolute value of γ, which ranges between 0 and 1, is the function of systemic spatial de-correlation (noise) and temporal de-correlation between the master and slave acquisitions (geometrical decorrelation and temporal decorrelation).

To extract damaged areas due to the Kumamoto earthquake, the coherence was obtained from the pre-event (April 15) and the post-event (April 29) SAR images, as the slant range complex data. In the calculation, 5 x 5 pixels' window was applied to the slant range. Then it was projected on the base map with the pixel size of 2.5 m. The coherence was calculated for the SAR image pair as shown in **Figure 4**. Note that in the figure, the distribution of the coherence was plotted only for urban land-cover (a) and the histogram of the coherence for the entire image pair (b).

LiDAR surveys were carried out for the affected areas along the causative faults by Asia Air Survey Co., Ltd. [20]. The density of the collected LiDAR data was 1.5 - 2 points/m^2 for the first flight on April 15, and 3 - 4 points/m^2 for the second flight on April 23 (**Figure 5a**). This LiDAR pair dataset is one of the few cases in which pre- and post-event digital surface models (DSMs) were obtained from the same airplane, instrument, and pilot.

The spatial correlation coefficient of the two LiDAR data was calculated using a 101 x 101 pixels window (50 m x 50 m), and the horizontal shift of the April-23 DSM with the maximum correlation coefficient was considered as the crustal movement by the April-16 main-

shock. The horizontal component of the calculated coseismic displacement was applied to the post-event DSM to cancel it, and then the vertical displacement between the two DSMs was calculated [21]. In this study, the both horizontal and vertical coseismic displacements were removed to extract collapsed build in the study area. **Figure 5b** shows the relative vertical displacement of the two DSMs from LiDAR data, where blue colored pixels show the decrease of height, mostly due to the collapse of buildings.

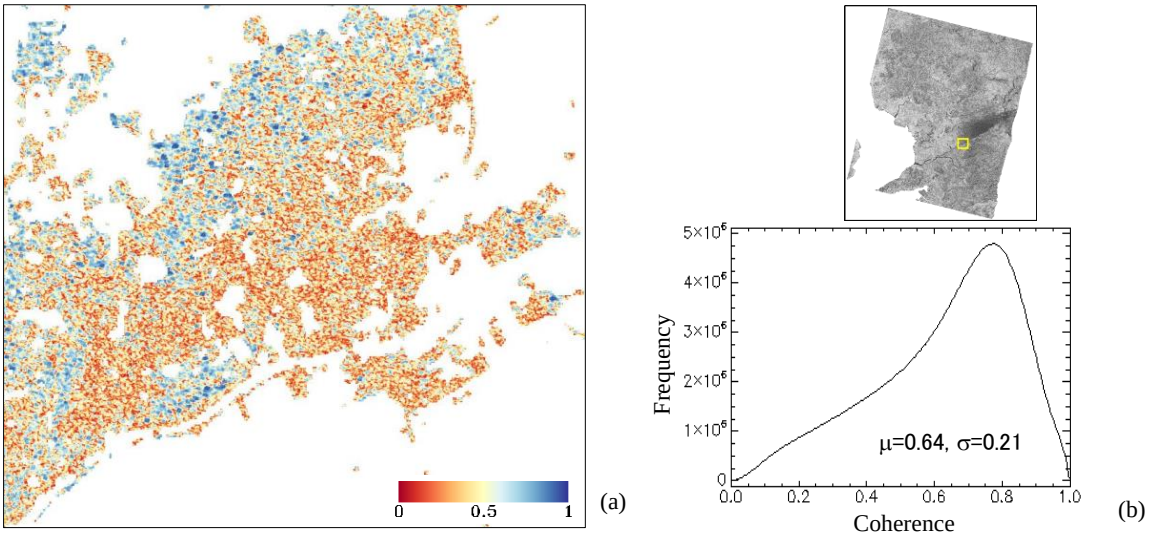

Figure 4: Coherence between the two PALSAR-2 images (2016/4/15 vs 2016/4/29) for the urban land-cover in the central Mashiki Town (a) and the histgram of the coherence for the entire image pair (b).

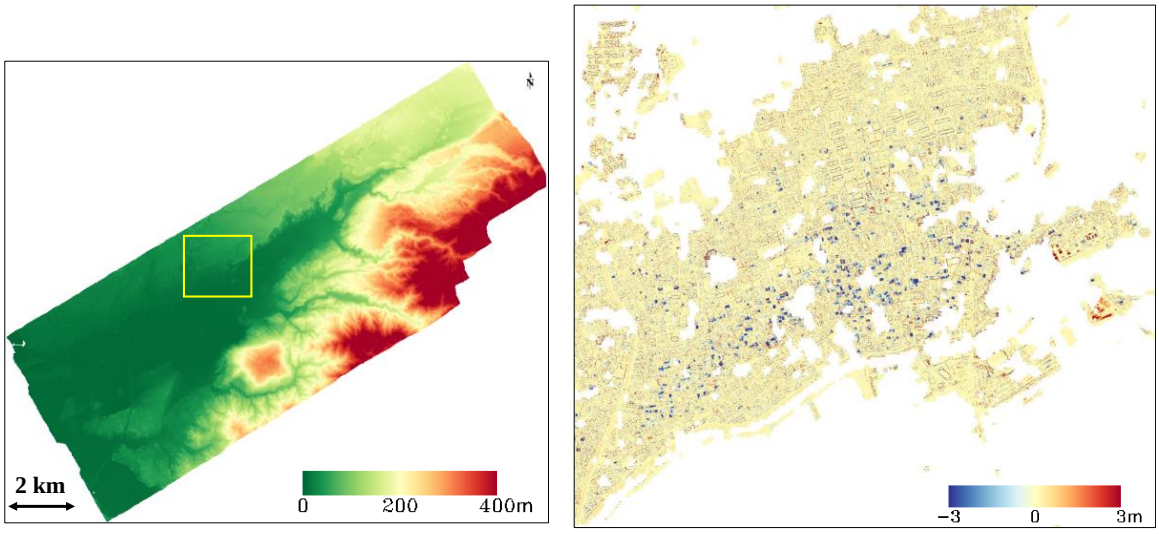

(a) (b)

Figure 5: DSM obtained from LiDAR flight on April 23, 2016 (a) and the difference of the two DSMs' heights in the study area after removing crustal movements (b).

5 Determination of Threshold Values

In order to extract the area of building collapse, the threshold value of the coherence in **Figure 4** must be determined properly. But it is not so easy to determine this value. Thus, the several coherence values were attempted as possible thresholds to extract building damage areas. **Figure 6a** shows the graph between the coherence threshold and the area and area-ratio

of extracted pixels (0.5 x 0.5 m^2) under each coherence value. Note that if $\mu \pm 2\sigma$, which is 0.22, is selected as the coherence threshold, about 11 % of the urban land-cover of the target area is extracted. If $\gamma < 0.2$ is used as the area selection criteria of low coherence, the extracted area becomes about 9 %.

In order to determine the coherence threshold, the difference of the LiDAR DSMs was considered. **Figure 6b** shows the relationship between the height difference and the extracted area exceeding the plus and minus thresholds. For example, if ± 0.5 m is selected as the height difference threshold, about 8.5 % of the target area is extracted. Note that although LiDAR DSMs have elevation accuracy of less than 10 cm, the location accuracy of laser cloud points is an order of 50 – 70 cm. Considering this situation, +0.5 m was determined as the height difference threshold of changes for 0.5-m square grid LiDAR data. It is recognized from the figure that the area of reduced-height pixels is about 1.6 times of the area of increased-height pixels. This observation can be explained by the fact that the reduced-height in this urban area is mostly due to the collapse of buildings and the increased-height is due to the accumulation of debris and the displacement of collapsed buildings to surrounding areas.

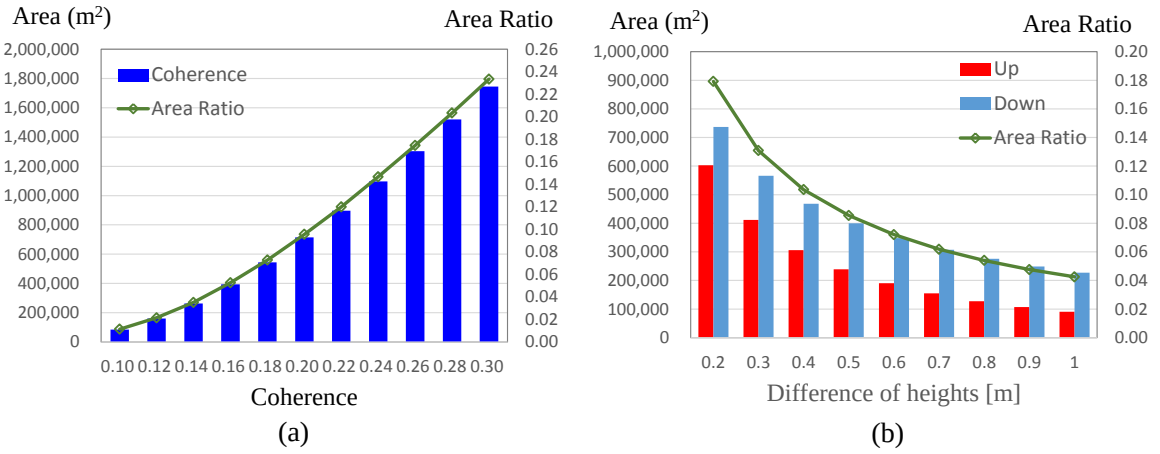

Figure 6: Relationship between the coherence and the extracted area by the coherence threshold (a); Relationship between the height difference and the area exceeding the plus and minus thresholds (b).

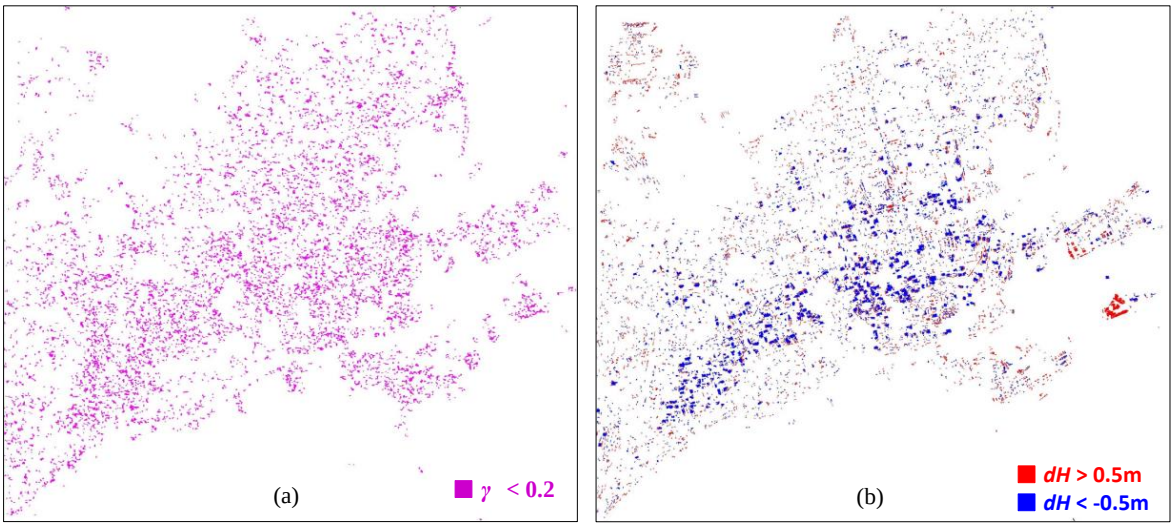

Figure 7: Changed areas extracted by low coherence ($\gamma < 0.2$) (a); Changed areas extracted by height-difference (abs. (dH) > 0.5 m) (b). Objects smaller than 9.0 m^2 were excluded as noises from these plots.

Figure 7 shows the possible changed areas extracted by low coherence ($\gamma < 0.2$) and those by height-difference ($dH > 0.5$ m or $dH < -0.5$ m). In these extractions, the objects smaller than 9.0 m^2 were removed as noises, such as cars and debris. The distributions of the extracted areas were not the same but very similar although the situations of change for the two data sets have some different aspects.

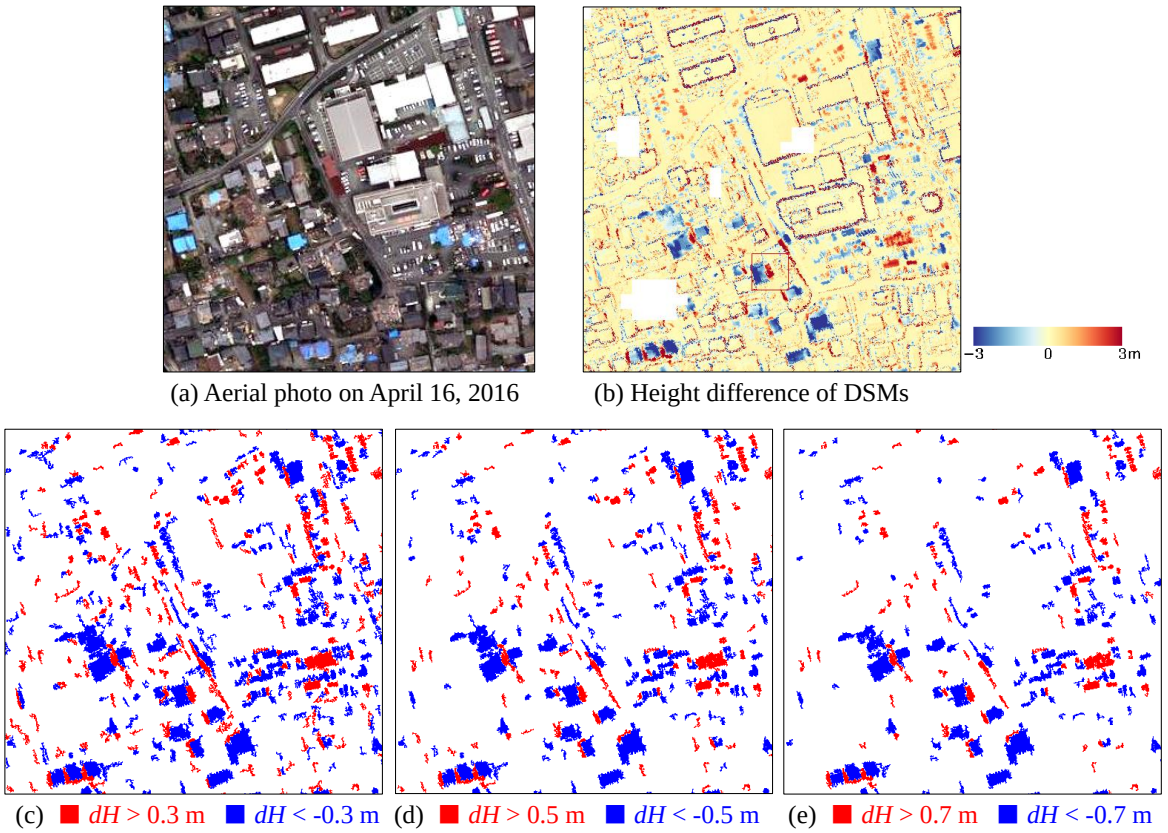

Figure 8: Aerial photograph around Mashiki Town office (a), height differnce of DSM (b), and extracted areas by different height-difference values (c-e). Objects smaller than 9.0 m^2 were excluded.

The extracted areas from the LiDAR DSMs were closely examined for a central part of Mashiki Town including the town office building in **Figure 8**. It is seen from the figure that by increasing the height-threshold, the selected areas are seen to decrease. Increased-height pixels are seen to be mostly parking cars and some debris while decreased-height pixels are collapsed buildings. Thus multi-temporal LiDAR data is considered to be very effective to extract heavily impacted urban areas due to natural disasters.

6 Conclusions

L-bans Synthetic Aperture Radar (SAR) imagery data acquired before and after the 2016 Kumamoto, Japan earthquake by PALSAR-2 sensor onboard ALOS-2 satellite were employed to extract building damage based on coherence values. The areas of urban land-cover were selected for the target of analysis since non-urban land-cover, such as vegetation, might be a cause of incoherence. Two temporal digital surface models (DSMs) obtained by LiDAR flights were also introduced as validation data of the change detection from the SAR data. Comparing these two data sets, the pixels of low coherence ($\gamma < 0.2$) from the two-temporal

SAR data and the pixels of height-difference (abs. (*dH*) > 0.5 m) from the LiDAR DSMs were considered as changed areas, mostly due to collapsed buildings and accumulated debris. A more detailed comparison with field survey data and aerial images will be provided in the near future.

.Acknowledgement

This study was conducted under financial supports of the J-RARID Kumamoto project of the Japan Science Technology Agency (JST) and the Grant-in-Aid for Scientific Research (Project Nos. 25242035, 15K16305) of the Japan Society for the Promotion of Science (JSPS). The ALOS-2 PALSAR-2 data used in this study are owned by Japan Aerospace Exploration Agency (JAXA), and were provided through JAXA's 4th ALOS-2 Research Announcement (RA-4), PI Number 1503 (F. Yamazaki). The LIDAR data used in this study were acquired and owned by Asia Air Survey Co., Ltd., Japan.

References

[1] F.Yamazaki. Applications of remote sensing and GIS for damage assessment. *Proceedings of the 8th International Conference on Structural Safety and Reliability*, CD-ROM, 12p, 2001.

[2] F. Yamazaki and M. Matsuoka. Remote sensing technologies in post-disaster damage assessment. *Journal of Earthquakes and Tsunamis*, Vol. 1, No. 3, 193-210, 2007.

[3] R.T. Eguchi, C. Huyck, S. Ghosh, B.J. Adams. The application of remote sensing technologies for disaster management. *The 14th World Conference on Earthquake Engineering*, CD-ROM, 2008.

[4] F. Dell'Acqua, P. Gamba. Remote sensing and earthquake damage assessment: Experiences, limits, and perspectives. *Proceedings of the IEEE* 100 (10), 2876-2890, 2012.

[5] N. Yague-Martinez, M. Eineder, X.Y. Cong, C. Minet. Ground displacement measurement by TerraSAR-X image correlation: The 2011 Tohoku-Oki Earthquake. *IEEE Geoscience and Remote Sensing Letters*, Vol. 9, No. 4, 539-543, 2012.

[6] W. Liu, F. Yamazaki, H. Gokon, S. Koshimura. Extraction of tsunami-flooded areas and damaged buildings in the 2011 Tohoku-Oki Earthquake from TerraSAR-X intensity images. *Earthquake Spectra*, 29(S1), S183-S200, 2013.

[7] P. Nakmuenwai, F. Yamazaki. Extraction of flooded areas in the 2011 Thailand flood from RADARSAT-2 and ThaiChote images. *Proc. of the IEEE 2014 International Geoscience and Remote Sensing Symposium*, Quebec, Canada, 3354-3357, 2014.

[8] E. Mas, J. Bricker, S. Kure, B. Adriano, C. Yi, A. Suppasri, S. Koshimura. Field survey report and satellite image interpretation of the 2013 Super Typhoon Haiyan in the Philippines. *Natural Hazards and Earth System Sciences*, 15, 805–816, 2015.

[9] F. Yamazaki, R. Bahri, W. Liu, T. Sasagawa. Damage extraction of buildings in the 2015 Gorkha, Nepal earthquake from high-resolution SAR data. *Proc. of SPIE*, Vol. 9877, 98772K-1-11, doi: 10.1117/12.2223306, 2016.

[10] F. Yamazaki, D. Suzuki, Y. Maruyama. Use of digital aerial images to detect damages due to earthquakes. *Proc. 14th World Conf. Earthquake Engineering*, Paper No. 01-1049, CD-ROM, 2008.

[11] T.T. Vu, F. Yamazaki, M. Matsuoka. Multi-scale solution for building extraction from LiDAR and image data. *International Journal of Applied Earth Observation and Geoinformation*, 11, 281–289, 2009.
[12] Cabinet Office of Japan. Summary of damage situation in the Kumamoto earthquake sequence, http://www.bousai.go.jp/updates/h280414jishin/index.html (Accessed Dec. 2016.)
[13] Japan Meteorological Agency. The number of aftershocks of recent inland earthquakes in Japan. http://www.data.jma.go.jp/svd/eqev/data/2016_04_14_kumamoto/kaidan.pdf (Accessed Dec. 2016.)
[14] Geospatial Information Authority of Japan. the 2016 Kumamoto Earthquake. http://www.gsi.go.jp/BOUSAI/H27-kumamoto-earthquake-index.html (Accessed Dec. 2016.)
[15] Y. Sakai. A Preliminary Report on the Strong Ground Motions during the Kumamoto Earthquake and Damage, http://www.kz.tsukuba.ac.jp/~sakai/kmm.htm (Accessed Dec. 2016) (in Japanese).
[16] F. Yamazaki, W. Liu, Remote sensing technologies for post-earthquake damage assessment: A case study on the 2016 Kumamoto earthquake, *6th Asia Conference on Earthquake Engineering*, Cebu City, Philippines, 13p, 2016.
[17] JAXA. Calibration Result of ALOS-2/PALSAR-2 JAXA Standard Products, http://www.eorc.jaxa.jp/ALOS-2/en/calval/calval_index.htm (Accessed Dec. 2016)
[18] JAXA. High-resolution land-use and Land-cover map of Japan, http://www.eorc.jaxa.jp/ALOS/lulc/jlulc_jpn.htm (Accessed Dec. 2016)
[19] A. Ferretti, A. Monti-Guarnieri, C. Prati, F. Rocca. Part C InSAR processing: a mathematical approach, In InSAR Principles: *Guidelines for SAR Interferometry Processing and Interpretation*, K. Fletcher, Ed., ESA Publications: Noordwijk, Netherlands, pp. 3-13, 2007.
[20] Asia Air Survey Co., Ltd. the 2016 Kumamoto Earthquake. An approach of crustal deformation analysis based on comparison of two periods of Lidar measurement. http://www.ajiko.co.jp/article/detail/ID5725UVGCD/ (Accessed Dec. 2016)
[21] L. Moya, F. Yamazaki, W. Liu, T. Chiba, Calculation of coseismic displacement from Lidar data in the 2016 Kumamoto, Japan, earthquake, Natural Hazards and Earth System Sciences, Discussion paper, doi:10.5194/nhess-2016-315, 2016.